Received: 15 March 2024 | Accepted: 2 April 2024

DOI: 10.1002/maco.202414388

ARTICLE

Materials and Corrosion

Mechanistic insights into chemical corrosion of AA1050 in ethanol-blended fuels with water contamination via phase field modeling

Eugen Gazenbiller[1] | **Visheet Arya**[2] | **Rüdiger Reitz**[2] | **Matthias Oechsner**[2] | **Mikhail L. Zheludkevich**[1,3] | **Daniel Höche**[1]

[1]Institute of Surface Science, Helmholtz-Zentrum Hereon, Geesthacht, Germany

[2]Institute for Materials Technology (IfW), Technische Universität Darmstadt, Darmstadt, Germany

[3]Faculty of Engineering, Kiel University, Kiel, Germany

Correspondence
Eugen Gazenbiller, Institute of Surface Science, Helmholtz-Zentrum Hereon, 21502 Geesthacht, Germany.
Email: eugen.gazenbiller@hereon.de

Funding information
Deutsche Forschungsgemeinschaft, Grant/Award Numbers: DFG HO4478/6-1, OE558/20-1, DFG HO4478/6-2, OE558/20-2

Abstract

Aluminum alloys are widely used in automotive construction, and since the introduction of biogenic ethanol into fuels, the issue of nonaqueous alcoholate corrosion has become an important topic. In this paper, the kinetics of AA1050 temperature-induced alcoholate pitting corrosion are examined experimentally with a specially constructed microreactor. The generated data are utilized to create a phase field model for the pit growth phase. The effects of ethanol-blend composition and water content are quantitatively assessed and simulated. Phase field simulations allow for the first time the mechanistic characterization of the chemical corrosion process with a water content of up to 0.3% and an estimation of relevant reaction parameters at temperatures of up to 150°C. The approach can further be utilized to develop strategies for minimizing corrosion risk in-service.

KEYWORDS

aluminum, finite element method, non-aqueous corrosion, phase field model

1 | INTRODUCTION

The transportation sector represents a significant contributor to CO_2 emissions, necessitating innovative approaches to mitigate greenhouse gas releases resulting from the combustion of fossil fuels. An established measure to address this challenge involves the incorporation of biogenic ethanol through fuel blending, a mandatory practice in countries such as Brazil. Despite the positive environmental impact, the heightened reactivity of alcohols in comparison to nonpolar hydrocarbons introduces potential corrosion concerns in automotive components, particularly evident in aluminum (Al) alloys. Recent literature has highlighted the susceptibility of Al alloys to "dry," water-free alcoholate pitting corrosion at elevated temperatures.[1–5] A key factor in this corrosion mechanism is the water content, as its reduction below a specific threshold triggers the initiation of pitting corrosion because it prevents repassivation of the oxide layer after pit initiation.[1,2] Despite the substantial progress made in interpreting the corrosion mechanism, the role of water in the growth stage remains unexplored in the existing literature.

In recent years, the possibility of simulating electrochemical localized corrosion using the phase field method has been explored.[6–10] Phase field modeling is

a versatile method for tracking moving interfaces. In contrast to sharp-interface approaches, different phases are described by means of the scalar phase field variable (or "order parameter"). Its spatial and temporal evolution is governed by a differential equation minimizing the system's free energy. A key advantage of the phase field approach is the continuous order parameter, which can handle discontinuities and topological changes more efficiently than sharp-interface formulations. Furthermore, explicit tracking of moving boundaries (such as in Eulerian or Lagrangian methods) is not necessary because it is part of the phase field solution. Phase field methods are based on a thermodynamic description of the system with the free energy playing a fundamental role in the mathematical formulation.

The most published phase field corrosion models make use of the thermodynamic framework and free energy formulation, which was introduced by Kim, Kim, and Suzuki for solidification of binary alloys.[11] The advantage of the approach is the fact that no boundary conditions have to be imposed at the electrolyte–solid boundary, and the transition from activation- to diffusion-controlled corrosion modes is captured automatically when the overpotential is sufficiently high. The system is characterized by two scalar order parameters c' and η (both between 0 and 1), which describe the normalized corroding ion concentration and the phase composition, respectively.

In general, phase field variables are subdivided into two categories: conserved and nonconserved. The temporal evolution of conserved order parameters is described by the Cahn–Hilliard equation. The Cahn–Hilliard equation is a stiff, nonlinear, fourth-order partial differential equation and was originally formulated to describe spinodal decomposition of a binary mixture.[12,13] In literature, it was successfully applied to simulate multiphase flow,[14] phase transformations,[15] and microstructural evolution[16] just to name a few. Evolution of nonconserved order parameters is described by the second-order parabolic Allen–Cahn equation, which is used for microstructure coarsening.[17] In most cases, phase field models consist of coupled conserved and nonconserved fields, so both equations are employed. An important advantage of the phase field method is the ability to intrinsically capture activation- and diffusion-controlled reaction modes, which was exploited in the course of this work.

Due to the scarcity of publications on alcoholate corrosion and corresponding critical parameters and mechanisms, we aim to develop a suitable phase field model to simulate the temperature-induced growth phase of AA1050 pitting corrosion and validate it with experimental data from a specially constructed microreactor. The paper is organized as follows: We introduce the utilized phase field model, including all governing equations, then describe the experimental methods, and further validate the model by comparing the experimental and simulated pit shapes at the examined fuel and water concentrations similar to in-service conditions and deducing mechanistic consequences for the corrosion reaction. Both the combination of phase field simulations and pit shape analysis and the proposition of a possible reaction mechanism of ethanolate corrosion of AA1050 are key novel aspects of this work.

2 | MODEL DESCRIPTION

Pitting processes are usually subdivided into initiation and growth. A statistical consideration of pit entirety on AA1050 in anhydrous ethanol was conducted in a previous work.[5] Here, we focus on the growth process of a single pit after the initiation event, which includes passive layer breakdown on lower time and length scales. The general corrosion reaction during pit growth can be represented by the chemical reaction equation (Equation 1)

$$\mathrm{Al} + 3\mathrm{C_2H_5OH} \rightarrow \mathrm{Al^{3+}} + 3\mathrm{C_2H_5O^-} + \frac{3}{2}\mathrm{H_2}. \quad (1)$$

Reaction (1) is expected to proceed chemically, that is, it can be characterized as a surface redox reaction and the anode and cathode are localized at the same spot. Indications for the feasibility of this assumption will be discussed in Section 4.1. The interfacial kinetics in such reactions is controlled either by activation or by diffusion. Compared to purely electrochemical processes, the driving force for the activation-controlled reaction is not overpotential but temperature. The rate constant of such reaction k_{pit} ($\mathrm{s^{-1}}$) is usually approximated by the Arrhenius equation (Equation 2)

$$k_{\mathrm{pit}} = A_{\mathrm{pre}} \exp\left(-\frac{E_A}{RT}\right), \quad (2)$$

where A_{pre} is a pre-exponential factor (also frequency factor), E_A is the activation energy, R is the universal gas constant, and T is the temperature. Although A_{pre} is reported to be a temperature-dependent value according to $A_{\mathrm{pre}} = A_0 T^n$ with $-1.5 < n < 2.5$, it is often assumed constant due to negligible errors for small temperature differences.[18] If the concentration of the surrounding reactant is high, the reaction becomes zeroth order and the reaction rate r_{pit} ($\mathrm{mol\,m^{-2}\,s^{-1}}$) is proportional to k_{pit}. At the same time, the temperature dependence of the diffusion coefficient is governed by the Stokes–Einstein relation (Equation 3):

$$\frac{D_{T_1}}{D_{T_2}} = \frac{T_1}{T_2}\frac{\mu_{T_2}}{\mu_{T_1}}, \tag{3}$$

where D_T are the diffusion coefficients and μ_T are the dynamic viscosities at a given temperature. The transition between activation- and diffusion-governed kinetics takes place when a salt layer forms at the pit surface. The formation depends on the solubility product of the salt, which itself is a temperature-dependent value. According to Wang et al.,[19] the temperature-dependent solubility of Al ethoxide in anhydrous ethanol (also referred to as E100) as molar fraction $x_{Al(EtO)_3}$ can be approximated analytically as

$$x_{Al(EtO)_3}(T) = \exp(71.604 - 5023.85/T - 11.450 \ln[T]) \tag{4}$$

from which the saturation concentration c_{sat} can be deduced. For water-containing fuels, possible precipitation of $Al(OH)_3$ is considered as an additional term, which contributes to c_{sat}.

The utilized phase field governing equations are based on the publications of Mai and Soghrati,[8] Ansari et al.,[7] and Cui et al.[20] A decisive parameter in all phase field models is the definition of the system free energy $\mathscr{F}$:

$$\mathscr{F} = \mathscr{F}_{bulk} + \mathscr{F}_{int} = \int [f(c', \eta) + f_{int}]dV, \tag{5}$$

where $f(c', \eta)$ is the bulk energy contribution, c' is the normalized metal concentration, η is the order parameter, and f_{int} is the interfacial contribution that can be written as

$$f_{int} = \frac{\alpha_\eta}{2}(\nabla\eta)^2, \tag{6}$$

where α_η is the gradient energy coefficient of the order parameter.

For the bulk energy calculation, the Kim–Kim-Suzuki approach for phase separation is applied to the present problem.[11] The electrolyte and alloy composition is described by the varying phase field variable η. The normalized metal (or ion) concentration c' in the interfacial region is expressed as

$$c' = h(\eta)c'_s + [1 - h(\eta)]c'_l, \tag{7}$$

where $h(\eta) = -2\eta^3 + 3\eta^2$ is an interpolation function and c'_s and c'_l are the normalized concentrations of solid and liquid phases, respectively. Considering an equilibrium between the solid and liquid phases chemical potentials $\frac{\partial f_s(c'_s)}{\partial c'_s}$ and $\frac{\partial f_l(c'_l)}{\partial c'_l}$, the bulk free energy density $f(c', \eta)$ can be written as (Equation 8)

$$f(c', \eta) = h(\eta)f_s(c'_s) + [1 - h(\eta)]f_l(c'_l) + wg(\eta), \tag{8}$$

where $g(\eta) = \eta^2(1-\eta)^2$ is the double-well potential with the height w. The free energy densities of both phases take the shape of

$$\frac{\partial f_s(c'_s)}{\partial c'_s} = A(c'_s - c'_{se}), \tag{9}$$

$$\frac{\partial f_l(c'_l)}{\partial c'_l} = A(c'_l - c'_{le}), \tag{10}$$

where $c'_{se} = 1$ and $c'_{le} = c_{sat}/c_{sol}$ are the normalized equilibrium concentration of the solid and liquid phases, respectively, and A is the energy density curvature.

With the above considerations, the temporal evolution of η and c' can be expressed as Allen–Cahn and Cahn–Hilliard equation, respectively,

$$\frac{\partial\eta(\mathbf{r}, t)}{\partial t} = -L_\eta\left(\frac{\delta\mathscr{F}}{\delta\eta} - \alpha_\eta\nabla^2\eta(\mathbf{r}, t)\right), \tag{11}$$

$$\frac{\partial c'(\mathbf{r}, t)}{\partial t} = \nabla \cdot D_{Al}(T)\nabla(c'(\mathbf{r}, t) - h(\eta)(c_{se} - c_{le}) - c_{le}), \tag{12}$$

where L_η is the interfacial mobility parameter and $D_{Al}(T)$ is the temperature-dependent diffusion coefficient of the metal cation in the liquid phase. In case of a chemical reaction, L_η depends on the temperature according to Arrhenius kinetics defined in Equation (2) in contrast to an electrochemical process where an overpotential-dependent Butler–Volmer-type equation has to be defined.[6] It can thus be stated as

$$L_\eta(T) = L_0\exp\left(-\frac{E_A}{RT}\right), \tag{13}$$

where L_0 is assumed constant like A_{pre} in Equation (2). This use of this equation for overall reaction rate approximation is only valid up to a certain water content and ion content, where electrochemical contribution is negligible. The exact value for the present system will be deduced in later sections and determines the validity domain of the model. The rate constant decrease due to hydrocarbon fuel addition to ethanol is modeled by adjustment of L_0.

In the classical phase field approach, the interface energy γ and interface thickness l are regarded as crucial model parameters. These can be related to the previously defined double-well potential w and the gradient energy coefficient α_η:

$$\gamma = 4\sqrt{w\alpha_\eta}, \tag{14}$$

$$l = \sqrt{2}a'\sqrt{\frac{\alpha_\eta}{w}}, \tag{15}$$

where $a' = 2.94$ for the interfacial region $0.05 < \eta < 0.95$.[11] In this work, however, we regard the parameters as purely numerical and do not interpret them considering their physical meaning.

Lastly, to compare the obtained simulated results with experimentally measured pits, we define an appropriate, novel error value σ_{error}, which combines the pit width (w) and depth (d) error into one value (Equation 16)

$$\sigma_{\text{error}} = \frac{\left(\sqrt{(d_{\text{sim}} - d_{\text{exp}})^2 + (w_{\text{sim}} - w_{\text{exp}})^2}\right)}{(w + d)/2}. \tag{16}$$

3 | METHODS

3.1 | Specimen preparation

Commercially available pure Al according to EN AW 1050A or UNS A91050 having 99.5% purity with the main alloying elements or impurities being Fe 0.32%, Si 0.06%, and Mn 0.04% was cut into a cylindrical shape. To achieve a homogeneous surface, it was mechanically ground using a well-lubricated silica wheel of grit P1000 at a considerably low speed, avoiding silica embodiment on the surface.

3.2 | Experimental

The corrosion experiments were conducted in a specially constructed pressure-proof reactor with a translucent window above the sample for identification of initiation events and growth progress. A schematic picture of the reactor is shown in Figure 1. The cylindrical alloy sample was placed at the bottom and the vessel was filled with either high-purity ethanol (Carl Roth ROTIPURAN® ≥ 99.8%, containing 0.03 ± 0.01 v/v% water, measured by Karl–Fischer titration) or with addition of a standardized reference fuel (Fuel C according to ASTM D 471 with 50% iso-octane and 50% toluene). The sample was heated, which induced the pitting corrosion reaction and accompanying hydrogen evolution. During the experiment, the temperature and pressure inside the vessel were logged with an accuracy of 0.1 bar and 0.1°C and the corrosion process was recorded by a video camera from above the reactor. The pressure was released after it reached a preset critical value so that the apparatus could cool down. After the reaction was completed, microscopic images were acquired for final pit depth and shape measurements.

3.3 | Simulation

The governing equations were implemented using Ritz–Galerkin approach of finite element method with six-node triangular Lagrangian elements (two-dimensional) for space

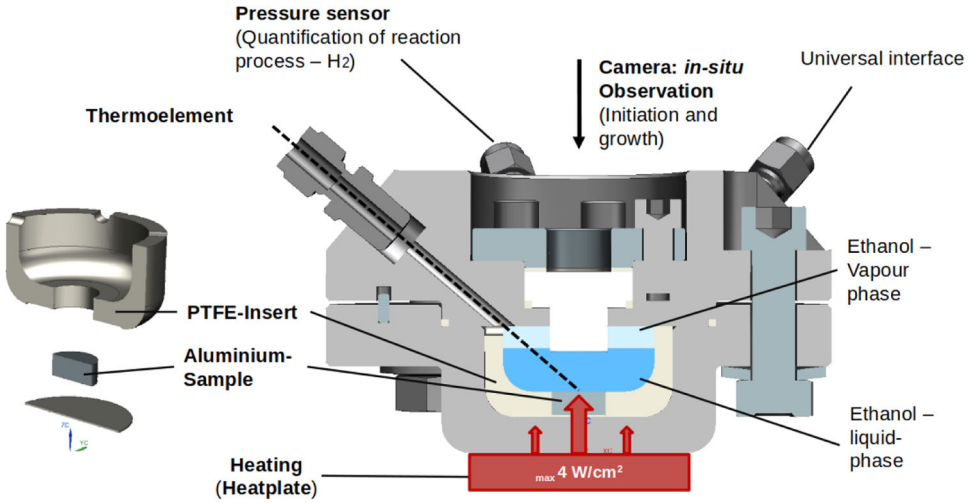

FIGURE 1 Schematic configuration of the utilized microreactor for alcoholate corrosion experiments. [Color figure can be viewed at wileyonlinelibrary.com]

discretization and generalized alpha method (also called θ method) for time integration due to very poor convergence with the backward differentiation Formula method. It was ensured that at minimum six elements are allocated in the transitional region for precise calculation of the order parameter gradient $\left(\frac{\delta \mathscr{F}}{\delta \eta}\right)$ and numerical stability by employing the technique of adaptive mesh refinement. The equation system was solved using a segregated Newton–Raphson scheme. The simulation domain was $5\,\text{mm} \times 10\,\text{mm}$ discretized with 320 000 triangular finite elements, as shown in Supporting Information S2: Figure A1. A Dirichlet-type constraint was imposed between the solid and liquid domains representing the passive oxide layer, apart from the initial semicircular pit opening in the domain center ($10\,\mu\text{m}$) The constraint was updated every timestep to simulate the continuous removal of the passive layer. The semicircular inset is not necessary; however, it significantly facilitates convergence at the beginning of the simulation. Initial conditions were: $c' = 0$ and $\eta = 0$ in the liquid domain and $c' = 1$ and $\eta = 1$ in the AA1050 alloy. Natural boundary conditions ($\frac{\partial c'}{\partial n} = 0$ and $\frac{\partial \eta}{\partial n} = 0$) were applied at all outer boundaries.

4 | RESULTS AND DISCUSSION

4.1 | Experimental observations and data acquisition

On an exemplary video recording (see Supplementary Information), it can be seen that random pit initiation events occur on the substrate surface when a critical temperature is reached. The consequent growth process is accompanied by rigorous hydrogen bubble formation and buoyancy from inside the pit. This indicates locally joint anodic and cathodic half-reaction. The conductivity of anhydrous ethanol without supporting electrolyte is very low, considering the autoprotolysis constant $pK_{ap,EtOH,25°C} = 16.2$,[21] which makes a chemical corrosion mechanism likely under present conditions. Consequently, the phenomenon of metastable pitting, that is, pits that stop growing because a certain aggressive environment cannot be sustained inside the pit, is not observed experimentally. In addition, the absence of water and oxygen in E100 makes the precipitation of a protecting oxide or hydroxide layer impossible. A possible formation of Al ethanolate, however, seems not to affect the reaction kinetics to a high degree, as will be shown in the next sections.

Another important observation is the behavior of the passive layer during the growth phase of the corrosion reaction. Some metals like iron exhibit formation of passive layer lacy covers above the growing pits in acidic aqueous electrolytes, that is, the protecting oxide detaches only partially and affects the ion transport inside the pit and thus the observed pit shape.[22] From our experimental observations, it can be stated that for AA1050 pitting corrosion in anhydrous ethanol, a complete passive layer detachment above the pit occurs during growth, which removed a diffusion barrier and has to be considered in the simulations. At this point, we note that the hydrogen bubble formation and buoyancy in the solution might lead to nonnegligible convective fluxes, which affect the mass transport in the solution. Consideration of this two-phase flow phenomenon requires to be dedicated additional experimental and modeling efforts and is not in the scope of the present study.

4.2 | Hypothetical pencil electrode test

The pencil electrode test is a popular experimental method to differentiate between diffusion and activation controlled reaction modes and determine corrosion kinetics and diffusion parameters. Furthermore, it is often used to verify computational corrosion models.[20,22] For a purely diffusion-controlled growth mechanism, the kinetic coefficient L_η has to be sufficiently large. We choose constant $L_\eta = 1 \times 10^6\,\text{m s kg}^{-1}$ and $D = 1 \times 10^{-10}\,\text{m}^2\,\text{s}^{-1}$ for the simulation.

As can be seen in Figure 2, the phase field model is able to capture diffusion-controlled growth, as indicated by the $\sqrt{t}$ pit depth dependence. A hypothetical temperature increase leads to a larger diffusion coefficient and a steeper slope of the depth versus time curve. However, this only applies if the kinetic coefficient L_η is kept constant. In reality, the temperature increase affects L_η too and the question, whether the diffusion coefficient or the kinetics rise is faster has to be answered. The issue is, however, the lack of literature on the relevant parameters like diffusion coefficients and activation energies. An attempt to derive an estimation of those parameters from experimentally generated data and a phase field modeling approach is shown in the next sections.

4.3 | Lateral pit kinetics in anhydrous E100

The novel reactor shown in Figure 1 allows visual in situ examination of the pit growth progress. In contrast to our first correspondence regarding alcoholate corrosion of AA1050,[5] where a larger "black-box" reactor and a statistical approach had to be utilized due to not precisely

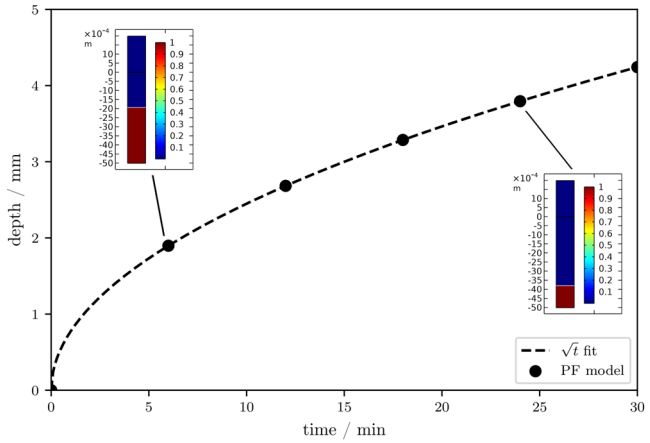

FIGURE 2 Demonstration of phase field model capabilities in simulating diffusion-controlled growth. Insets: Finite element model geometry of phase field model after 360 and 1440 s, respectively. [Color figure can be viewed at wileyonlinelibrary.com]

determinable pit initiation and times, this is a major improvement toward a physical description of the underlying process.

In Figure 3, micrographs of four specimens after reaction in anhydrous ethanol at different temperatures are shown. The surface of all specimens is damaged by several hemispherical pits, whereby in Figure 3b,c, most of the surface is covered by overlapped pits. Despite the overlaps, it is still clearly visible where the pits originated. It is remarkable that the pit shape is highly uniform on respective specimens. In electrochemical corrosion mechanisms without applied external potential, it is expected that existing pits affect the chemical environment and therefore subsequent pit growth kinetics, resulting in asymmetric pit shapes.[23]

The pit growth process was analyzed at four different temperatures: $T = 95°C$, 100°C, 110°C, and 120°C. The starting time was identified as the time when visible hydrogen evolution from the initiation site was detected. Three to five illustrative pit size developments are shown in Figure 4. These are also labeled in Figure 3. It is evident from Figure 4a–c that the lateral pit kinetics obey a linear relation at the observed temperatures. This fact indicates an activation-controlled reaction mechanism at the pit mouth because the radius of the pit is linearly correlated to the corroded volume per surface area. A higher temperature leads to a higher slope, as expected. A deviation from linear behavior is observed for reaction at $T = 120°C$ in Figure 4d. Here, the graphs have a parabolic dependence on time. This can be explained by the exothermic characteristics of the chemical corrosion reaction. At the high temperature, the kinetics become very high, leading to a rapid enthalpy release that cannot dissipate into the environment sufficiently fast, which leads to a local temperature rise and accelerates the reaction. It can be regarded as an example of a self-accelerating process.

At this point, the apparent lateral kinetics can be compared to our previous study, where the kinetics were estimated via a statistical approach in a black-box reactor.[5] At 110°C, the statistical method resulted in a lateral coefficient of 0.103 mm min^{-1} compared to the current study with 0.070 mm min^{-1}. The overestimation of approximately one-third is a consequence of the equalization of pit initiation with a pressure increase in the previous study, which is a considerable error source. Therefore, we can conclude that the first pits initiate before the measurable pressure rise, as also expected by the authors.[5]

4.4 | Pit depth versus lateral size: Mechanism indications

During pit growth, the time-dependent pit shape can give indications toward the underlying reaction mechanism. In particular, the ratio of observed lateral and depth kinetics is determined by the extent of diffusion contribution to the dissolution process. These conclusions were drawn and shown experimentally and by simulations for aqueous Fe alloy systems,[24] but the principles generally apply to any pitting corrosion reactions. It is observed that shallow pits form when the corrosion reaction is diffusion-controlled, whereas perfectly hemispherical pits are expected when it is activation-controlled. It must be noted that these considerations are only valid if the passive layer is weak, which means it dissolves (or is detached) during pit growth without creating an occluded volume underneath itself.

To reproduce the pit shapes and kinetics at the examined temperatures, the Allen–Cahn and Cahn–Hilliard (Equation 11) parameters have to be set. The most crucial ones are the kinetic coefficient L_η and the diffusion coefficient D_{Al}. We assume $D_{Al^{3+},25oC,EtOH} = D_{Al^{3+},25oC,H_2O} = 0.541 \times 10^{-9}\,m^2\,s^{-1}$ due to lack of literature data.[25] Although the solvation of the cation is expected to differ significantly compared to water, the precise value does not affect the simulation outcome in case of an activation-controlled mechanism. To estimate the kinetic coefficient L_η, the temperature dependence of the lateral pit kinetics (Figure 4) was analyzed under the assumption of an activation-controlled mechanism due to experimental observations. The graphical representation of the logarithmic Arrhenius equation is shown in Figure 5. From the slope of the linear fit and the interception with y-axis, an activation energy $E_A = 78.5 \pm 0.9\,kJ\,mol^{-1}$ and empirical pre-exponential factor $A_{pre} = 5.8 \pm 0.1 \times 10^7\,mol\,m^{-2}\,s^{-1}$ were

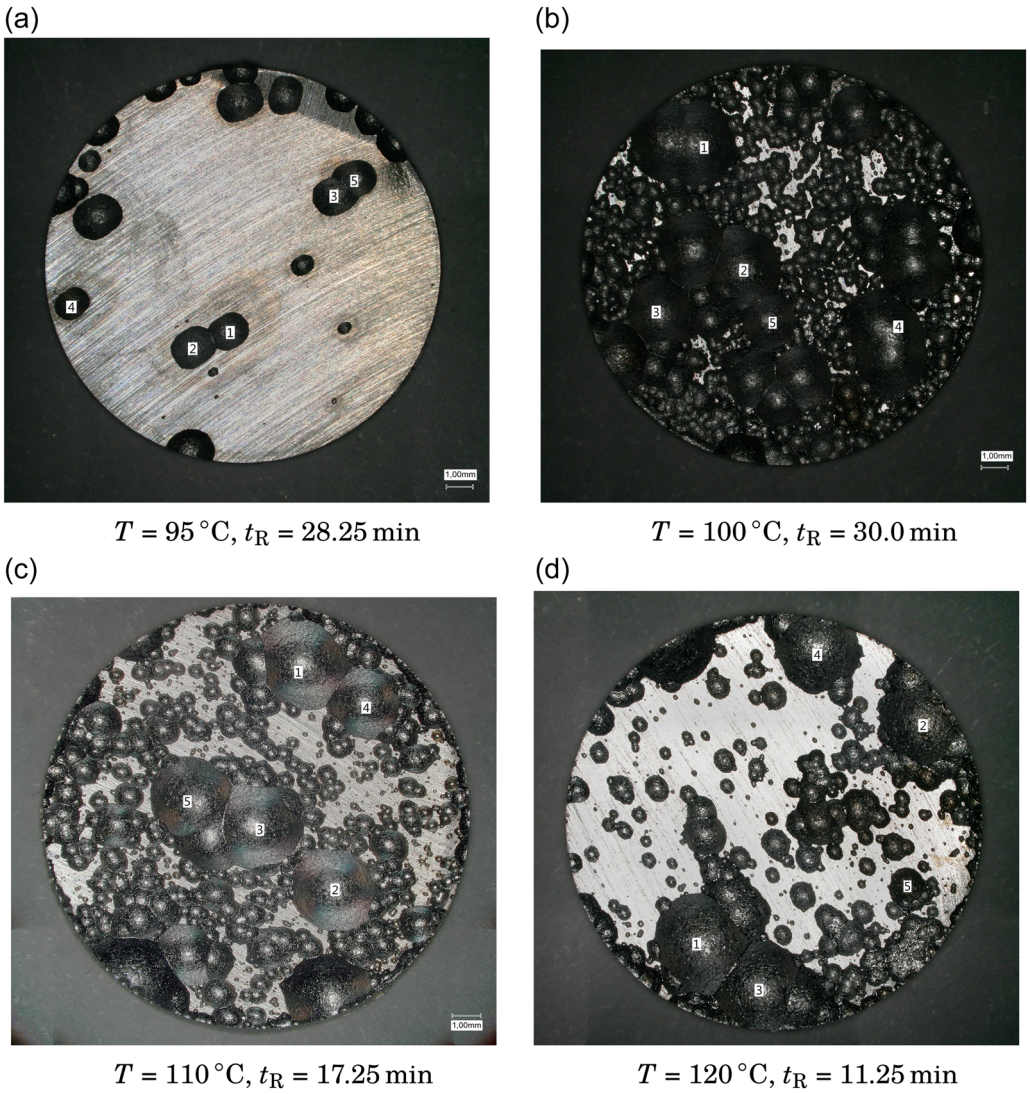

FIGURE 3 Exemplified optical micrographs of four specimens after reaction at increasing temperatures T (95–120°C; a–d) in anhydrous E100 for different reaction times t_R. The surfaces of all specimens were attacked by the surrounding liquid to a different degree. The scale bars correspond to 1 mm. Kinetics of annotated pits were further analyzed via video recordings for phase field model development.

determined. Both parameters are transferred to the definition of L_η, whereby A_{pre} is linearly proportional to L_0.

Following the model calibration, the simulation was performed by varying the temperature. The phase field parameter η distribution (which indicates the solid and liquid phases) after 10 min reaction time is shown in Figure 6. It is evident that the phase field model is able to reproduce the temperature dependence of the pit growth kinetics qualitatively. For a quantitative comparison, the experimental normalized and averaged pit widths and depths were compared to the simulations. The pit width and depth were probed during the simulations and are plotted in Figure 7. The pit depths are always slightly lower than the half-widths, which implies that there is slight diffusion control at the pit bottom. It was reported that the switch from activation to diffusion-controlled modes occurs gradually in case of electrochemical corrosion.[8,20] Mathematically, it is a shift from t^1 to $t^{0.5}$ dependence. This is difficult to measure experimentally, especially if data are only available for later stages of the reaction due to limitations of the measuring device like in this study.

For model validation, the width-to-depth ratios of selected pits after reaction (*post mortem*) were plotted together with the simulated ratios in Figure 8. A good agreement between the values at all three temperatures indicates the choice of an appropriate model framework and fitting parameters. It is worth noting that at $T = 120$°C (Supporting Information S2: Figure A2), the width-to-depth ratio of larger pits deviates from the perfect semicircle to a larger extent compared to smaller pits. It is an indication of an increasing diffusion control at the pit depth with advancing time. The obtained model results are used as a

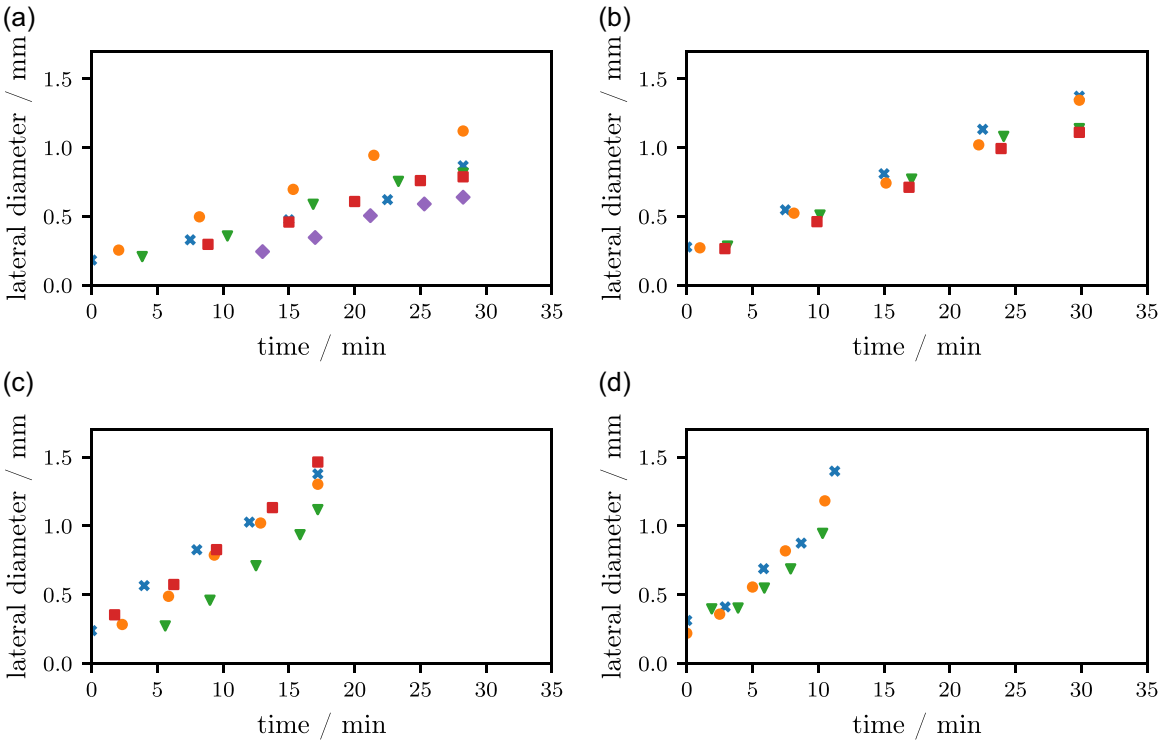

FIGURE 4 Visual examination of lateral pit kinetics in anhydrous E100 at (a) $T = 95°C$, (b) $T = 100°C$, (c) $T = 110°C$, and (d) $T = 120°C$. [Color figure can be viewed at wileyonlinelibrary.com]

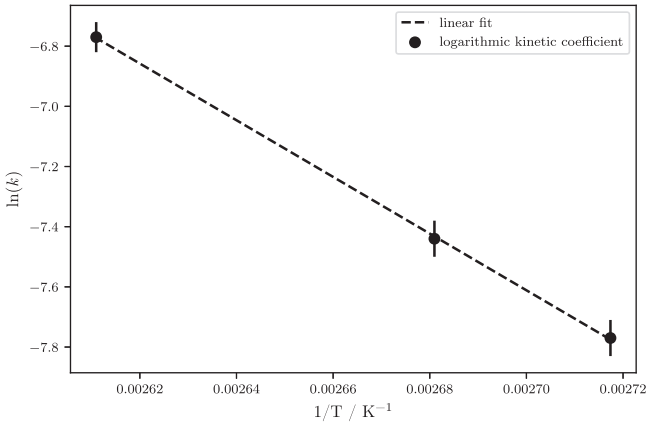

FIGURE 5 Arrhenius plot of activation controlled kinetic coefficient k at $T = 95°C$, 100°C, and 110°C in pure ethanol. Data from experiments at $T = 120°C$ was not utilized due to self-accelerated reaction mechanism.

reference for further model modification to include fuel and water effects in the subsequent section.

4.5 | Effect of fuel and water addition

The continuation of the experimental efforts with the addition of standardized fuel (80%, 70%, 60%, and 50%) and water (0.1% and 0.3%, respectively) to E100 enabled the interpretation of their effects on the pit growth phase. The clearly observed effects on the pitting initiation times are not part of this work and will be discussed in a future contribution by employing machine learning methods. The addition of fuel enables a more realistic environment in automotive applications, as E100 fuels are not common in the world market. To further simulate realistic conditions, the fuels were contaminated with defined concentrations of water (0.1% and 0.3%). This range is not arbitrary and was chosen because the experimental observations revealed a switch of mechanisms above 0.4% water. The increased measured overall growth kinetics and presence of secondary pits suggest that chemical corrosion is overlapped by electrochemical corrosion due to the increased conductivity of the ethanol–fuel mixture. Similar experimental findings were reported for other Al alloys, although they were not clearly interpreted in that context.[1] This aspect was not included in the present phase field model and is the subject of future studies.

The initiation at approximately 150°C did not lead to transition to a self-accelerating mechanism in the fuel-containing electrolytes, in contrast to E100, where it occurred already above 120°C. This suggests that the released thermal energy per time interval is lower, which facilitates temperature dissipation and impedes the transition to an uncontrolled reaction mode. The addition of fuel

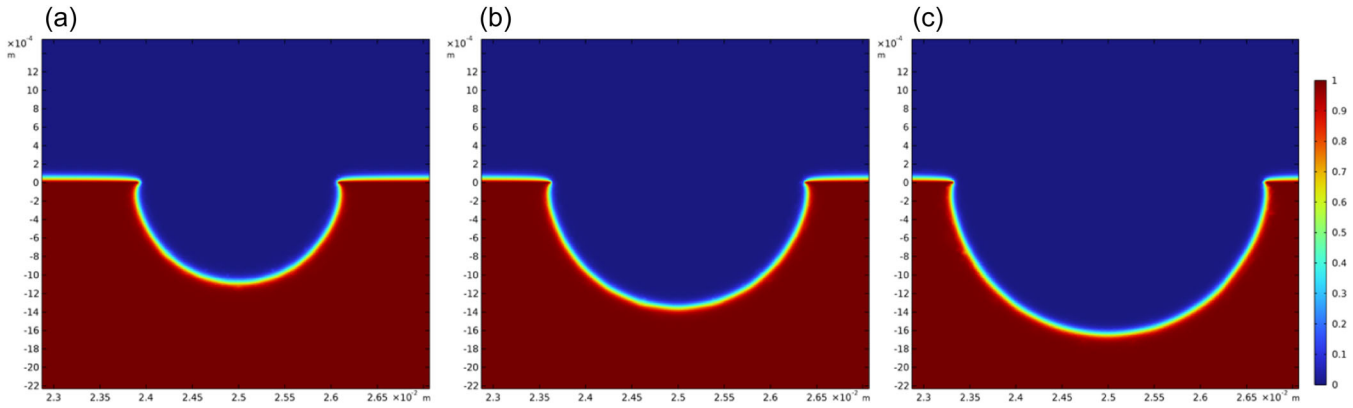

FIGURE 6 Distribution of phase field parameter η of simulated pits after 10 min reaction time in anhydrous E100 at (a) 95° C, (b) 100° C, and (c) 110° C. [Color figure can be viewed at wileyonlinelibrary.com]

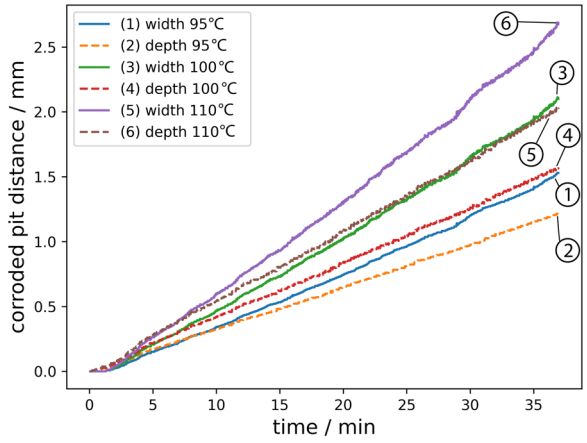

FIGURE 7 Pit width and depth probes taken during phase field simulations at different temperatures in anhydrous E100. [Color figure can be viewed at wileyonlinelibrary.com]

decreases the apparent reaction kinetics L_η, which reduces the released exothermic energy per time unit, and thus allows the reaction to occur in a non-self-accelerating manner at higher temperatures. The higher temperature compared to experiments in anhydrous E100, however, was necessary to ensure pit initiation due to the presence of water, which acts as an inhibitor.

To reproduce the time-dependent AA1050 pit shapes and sizes in the fuel- and water-containing ethanol within the developed phase field model, the kinetic coefficients, diffusion coefficients and solubility products were adjusted according to Table 1. The phase field model results are presented as corroded width and depth depending on reaction time in Figure 9.

The interpretation of the observed results and simulations allows formulation of the following mechanism: The addition of hydrophobic fuel and small amounts of water to the ethanol enables the formation of Al hydroxide and decreases the diffusion coefficient of Al^{3+} in the liquid phase. The facilitated formation and precipitation of the diffusion-limiting $Al(OH)_3$ salt via the proton-transfer reaction

$$Al(EtO)_3 + 3H_2O \rightarrow Al(OH)_3\downarrow + 3EtOH \quad (17)$$

quickly leads to a diffusion-controlled reaction at the pit bottom. Therefore, the pit aspect ratio decreases because the protecting salt precipitates earlier and prevents the metal ions from diffusing from the reacting surface, which results in wider pits compared to anhydrous E100. A larger fuel concentration leads to an enhancement of the effects, that is, a decrease of L_η, $D_{Al^{3+}}$ and the saturation concentration c_{cat} (which ideally is proportional to the solubility product of $Al(OH)_3$). However, it should be noted that the saturation concentration is a superposition of all precipitating salts, possibly including partially hydrolyzed species with chemical formulas $Al_x(EtO)_y(OH)_z$[26]; however, assessing their individual effects requires significantly broader theoretical knowledge about their properties and precipitation dynamics. The effect is therefore implemented in a simplified manner as a combined contribution of all precipitating salts ($c_{sat,salts,150°C}$).

Based on the obtained results, the following reaction pattern can be formulated for alcoholate corrosion of AA1050 at 150°C: In general, pit growth kinetics unsurprisingly decrease in ethanol–fuel mixtures with decreasing ethanol content. Between 0.1% and 0.4% water content, possible precipitation of Al hydroxide at the pit surface and consequent diffusion control slows down the pit growth. Furthermore, within the same ethanol concentration, an increase of water content leads to a decrease of the apparent diffusion coefficient $D_{Al^{3+}}$. This can partially be explained by the increase of

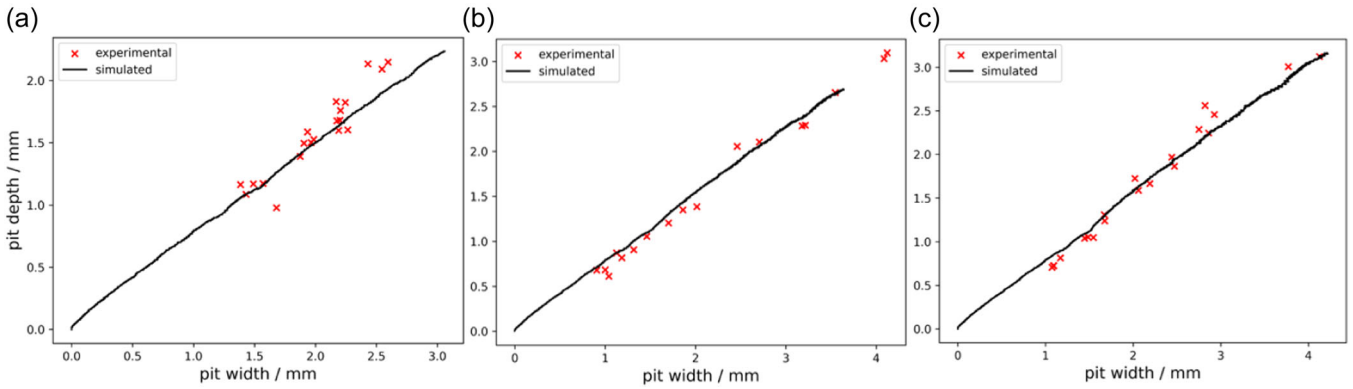

FIGURE 8 Experimentally measured pit widths and depths in anhydrous E100 at (a) 95°C, (b) 100°C, and (c) 110°C compared to phase field simulations. [Color figure can be viewed at wileyonlinelibrary.com]

TABLE 1 Phase field model parameters for defined fuel–ethanol–water mixtures.

Ethanol (vol%)	Water (vol%)	$L_{0,\,150°C}$ $(\mathrm{m\,s\,kg^{-1}})$	$D_{Al^{3+},\,150°C}$ $(\mathrm{m^2\,s^{-1}})$	$\frac{c_{salts,\,150°C}}{c_{solid}}$	$\bar{\sigma}_{error}$ (%)
20	0.1	1.5×10^{5}	1.3×10^{-8}	0.12	8.2
	0.3		0.6×10^{-8}	0.10	5.1
30	0.1	1.8×10^{5}	2.0×10^{-8}	0.15	7.4
	0.3		1.2×10^{-8}	0.10	9.1
40	0.1	2.4×10^{5}	2.2×10^{-8}	0.29	8.4
	0.3		1.6×10^{-8}	0.25	6.6
50	0.1	2.7×10^{5}	4.1×10^{-8}	0.34	6.9
	0.3		2.6×10^{-8}	0.27	5.8

electrolyte viscosity, as was reported in literature for ethanol–fuel mixtures,[27] but also by the fact that the diffusion is affected by the precipitated hydroxide layer. Increasing the water content above 0.5% leads to additional electrochemical corrosion contribution, which increases the overall observed kinetics and results in formation of secondary pits. The electrochemical contribution outweighs the diffusion coefficient decrease. Water concentration above 1% leads to suppression of the corrosion reaction because it enables repassivation of Al alloy and reconstruction of the native oxide layer. (Compare the exemplary microscopic images of AA1050 in E50 fuel with different water contamination in Supporting Information S2: Figure A3.) The interpretation is supported by the phase field model, which is able to reproduce the time-dependent pit shapes with reasonable errors by adjusting the crucial model parameters within the interpretation frame.

Obviously, the critical concentrations will change with varying temperature; however, considerations of all possible parameter permutations inside relevant ranges would require precise theoretical values and numerous additional experiments. This would also enable deducing concentration-dependent equations, which govern the phase field parameters, and gaining additional mechanistic insights. Nonetheless, the study demonstrates the ability of the chosen phase field model framework to handle this complicated phenomenon and to aid mechanistic interpretations.

5 | CONCLUSION

In this study, the growth phase of chemical alcoholate pitting corrosion of AA1050 in E100 and ethanol-blended fuels with water addition was examined experimentally and numerically for the first time. The pit growth phase was modeled via Allen–Cahn and Cahn–Hilliard equations, which were solved by the finite element method. The required data for model calibration was generated by

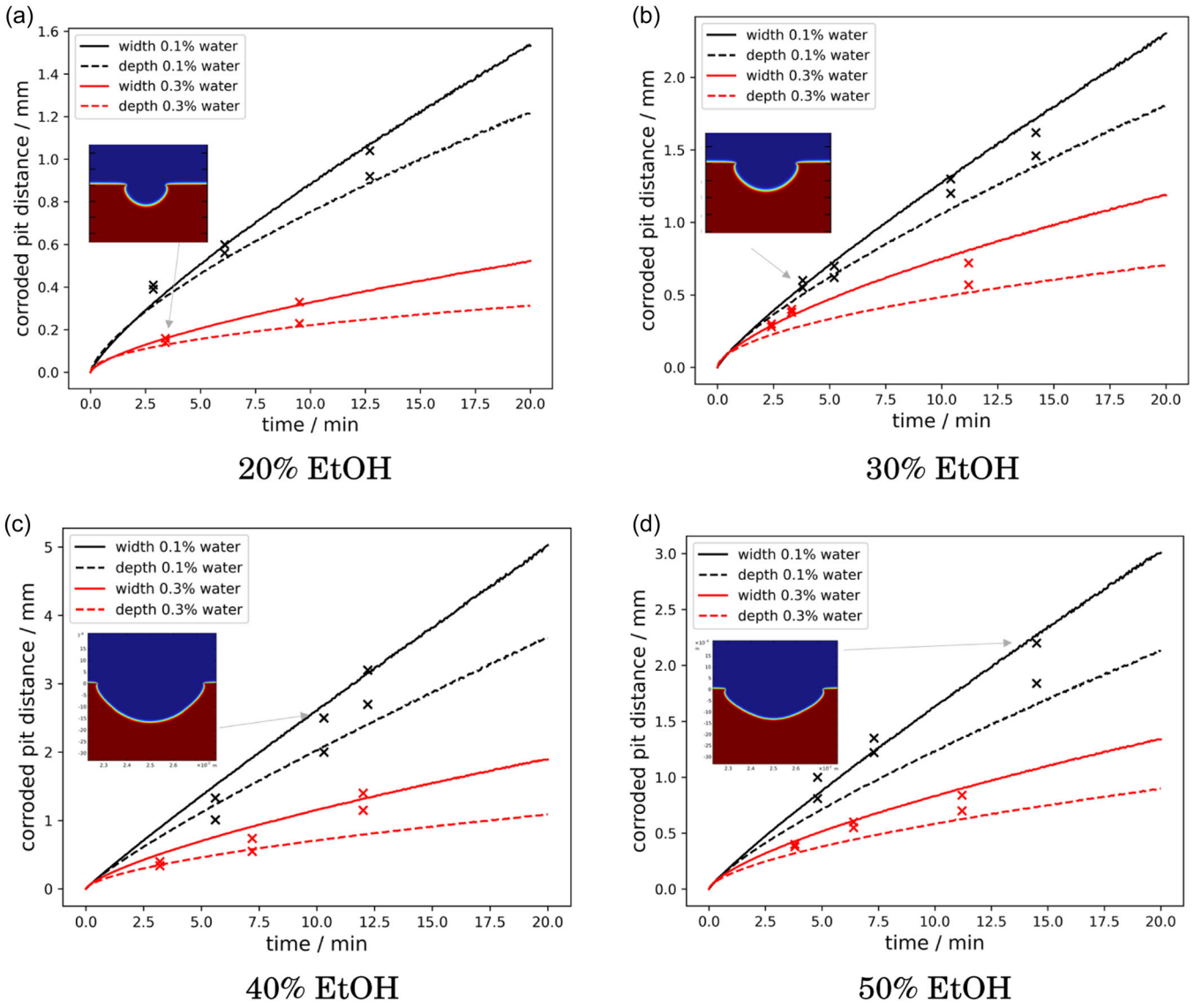

FIGURE 9 Simulated pit widths and depths for different ethanol concentrations (20%–50%; a–d) with parameters from Table 1 (solid and dashed lines) and experimentally determined values (cross symbols) for model validation. Insets: Phase field model results of selected pits, indicated by arrows. [Color figure can be viewed at wileyonlinelibrary.com]

a specially constructed reactor, facilitating visual in situ observation of the pit growth process. The approach allowed a simulative reproduction of pit shapes by introducing phase field variables related to the chemical reaction dynamics. The results demonstrate the chemical characteristics of the corrosion reaction and the effects of fuel-to-ethanol-ratio and water on the pit growth kinetics. The following key points can be deduced from the results:

- Alcoholate pitting corrosion of AA1050 in pure anhydrous ethanol (E100) propagates between 95°C and 110°C according to an activation-controlled chemical mechanism with an apparent activation energy $E_A = 78.5 \pm 0.9\ \mathrm{kJ\ mol^{-1}}$.
- Experiments in ethanol-blended fuels with water concentrations between 0.1% and 0.3% resulted in higher required initiation temperature, but lower pit growth kinetics and higher pit aspect ratios (width-to-depth) compared to anhydrous E100. Pit growth kinetics entered diffusion-controlled mode faster with increasing water concentrations, which is justified by possible precipitation of Al hydroxide. It exhibits an additional protective effect and influences the observed pit shapes.
- The water content plays a decisive role not only in the pit initiation process (by suppressing the initiation process at concentrations above 1% at 150°C) but also in the pit growth kinetics at 150°C by decreasing the apparent Al^{3+} diffusion coefficient.

- The limitations of the developed pit growth model lay in the fact that it does not include the pit initiation, which is mostly the limiting factor in the overall corrosion process. Furthermore, it is only applicable for fuels with less than 0.5% water at 150°C because it does not consider potential-dependent (electrochemical) corrosion contribution.

ACKNOWLEDGMENTS

The authors acknowledge the financial support by the Deutsche Forschungsgemeinschaft (DFG HO4478/6-1, OE558/20-1, DFG HO4478/6-2, OE558/20-2). Open Access funding enabled and organized by Projekt DEAL.

CONFLICT OF INTEREST STATEMENT

The authors declare no conflict of interest.

DATA AVAILABILITY STATEMENT

The raw/processed data required to reproduce the presented findings will be made available on reasonable request.

ORCID

Eugen Gazenbiller http://orcid.org/0000-0002-6361-4275

REFERENCES

[1] L. Krüger, F. Tuchscheerer, M. Mandel, S. Müller, S. Liebsch, *J. Mater. Sci.* **2012**, *47*, 2798.
[2] F. Tuchscheerer, L. Krueger, M. Mandel, S. Mueller, S. Liebsch, *Materialwiss. Werkst.* **2013**, *6*, 555.
[3] J. K. Thomson, S. J. Pawel, D. F. Wilson, *Fuel* **2013**, *111*, 592.
[4] L. Calabrese, P. Bruzzaniti, E. Proverbio, *Mater. Corros.* **2018**, *69*, 1815.
[5] E. Gazenbiller, V. Arya, R. Reitz, T. Engler, M. Oechsner, D. Höche, *Corros. Sci.* **2021**, *179*, 109137.
[6] L. Liang, Y. Qi, F. Xue, S. Bhattacharya, S. J. Harris, L.-Q. Chen, *Phys. Rev. E* **2012**, *86*, 051609.
[7] T. Q. Ansari, Z. Xiao, S. Hu, Y. Li, J.-L. Luo, S.-Q. Shi, *npj Comput. Mater.* **2018**, *4*, 38.
[8] W. Mai, S. Soghrati, *Electrochim. Acta* **2018**, *260*, 290.
[9] T. T. Nguyen, J. Bolivar, Y. Shi, J. Réthoré, A. King, M. Fregonese, J. Adrien, J.-Y. Buffiere, M.-C. Baietto, *Corros. Sci.* **2018**, *132*, 146.
[10] C. Tsuyuki, A. Yamanaka, Y. Ogimoto, *Sci. Rep.* **2018**, *8*, 12777.
[11] S. G. Kim, W. T. Kim, T. Suzuki, *Phys. Rev. E* **1999**, *60*, 7186.
[12] J. W. Cahn, J. E. Hilliard, *J. Chem. Phys.* **1958**, *28*, 258.
[13] J. W. Cahn, *Acta Metall.* **1961**, *9*, 795.
[14] F. Boyer, *Comput. Fluids* **2002**, *31*, 41.
[15] S. Y. Hu, L. Q. Chen, *Acta Mater.* **2001**, *49*, 1879.
[16] L.-Q. Chen, *Annu. Rev. Mater. Res.* **2002**, *32*, 113.
[17] S. M. Allen, J. W. Cahn, *Acta Metall.* **1979**, *27*, 1085.
[18] J. Cai, R. Liu, Y. Wang, *Solid State Sci.* **2007**, *9*, 421.
[19] W. Wang, Y. Zhang, Y.-Y. Wang, W. Tang, *J. Chem. Eng. Chin. Univ.* **2015**, *29*, 1293.
[20] C. Cui, R. Ma, E. Martínez-Pañeda, *J. Mech. Phys. Solids* **2021**, *147*, 104254.
[21] *CRC Handbook of Chemistry and Physics* (Ed: J. Rumble), 104 ed., CRC Press, London **2023**.
[22] P. Ernst, N. J. Laycock, M. H. Moayed, R. C. Newman, *Corros. Sci.* **1997**, *39*, 1133.
[23] M. I. Suleiman, R. C. Newman, *Corros. Sci.* **1994**, *36*, 1657.
[24] S. Scheiner, C. Hellmich, *Comput. Methods Appl. Mech. Eng.* **2009**, *198*, 2898.
[25] D. E. Gray, *American Institute of Physics Handbook*, McGraw Hill Higher Education, Maidenhead **1972**.
[26] R. C. Wilhoit, J. R. Burton, F. Kuo, S.-R. Huang, A. Viquesnel, *J. Inorg. Nucl. Chem.* **1962**, *24*, 851.
[27] S. A. Shirazi, B. Abdollahipoor, J. Martinson, K. F. Reardon, B. C. Windom, *Ind. Eng. Chem. Res.* **2018**, *57*, 11239.

SUPPORTING INFORMATION

Additional supporting information can be found online in the Supporting Information section at the end of this article.

How to cite this article: E. Gazenbiller, V. Arya, R. Reitz, M. Oechsner, M. L. Zheludkevich, D. Höche, *Mater. Corros.* **2024**, *75*, 1216–1227. https://doi.org/10.1002/maco.202414388